

Provable Preconditioned Plug-and-Play Approach for Compressed Sensing MRI Reconstruction

Tao Hong, *Member, IEEE*, Xiaojian Xu, *Member, IEEE*, Jason Hu, *Student Member, IEEE*,
and Jeffrey A. Fessler, *Fellow, IEEE*

Abstract—Model-based methods play a key role in the reconstruction of compressed sensing (CS) MRI. Finding an effective prior to describe the statistical distribution of the image family of interest is crucial for model-based methods. Plug-and-play (PnP) is a general framework that uses denoising algorithms as the prior or regularizer. Recent work showed that PnP methods with denoisers based on pretrained convolutional neural networks outperform other classical regularizers in CS MRI reconstruction. However, the numerical solvers for PnP can be slow for CS MRI reconstruction. This paper proposes a preconditioned PnP (P²nP) method to accelerate the convergence speed. Moreover, we provide proofs of the fixed-point convergence of the P²nP iterates. Numerical experiments on CS MRI reconstruction with non-Cartesian sampling trajectories illustrate the effectiveness and efficiency of the P²nP approach.

Index Terms—Preconditioner, plug-and-play (PnP), magnetic resonance imaging (MRI), reconstruction, Non-Cartesian sampling.

I. INTRODUCTION

MAGNETIC resonance imaging (MRI) is a noninvasive medical imaging technique that uses magnetic fields to obtain images of organs, tissues, and other structures. MRI scanners acquire the Fourier components of the image of interest, called the k-space. However, the whole acquisition procedure is slow. To accelerate the acquisition, one strategy is to under-sample the Fourier components, but this violates the condition of the Nyquist sampling theorem, causing aliasing in conventionally reconstructed images. To solve this problem, modern MRI scanners use multiple coils (parallel imaging) to acquire the Fourier components, providing additional spatial information [1–3]. Moreover, compressed sensing (CS) MRI [4, 5] improves the quality of the reconstructed images by using suitable sampling patterns. In practice, CS MRI is combined with parallel imaging and the MRI image is reconstructed by solving a composite minimization problem like the following:

$$\hat{\mathbf{x}} = \arg \min_{\mathbf{x} \in \mathbb{C}^N} \underbrace{\frac{1}{2} \|\mathbf{A}\mathbf{x} - \mathbf{y}\|_2^2}_{f(\mathbf{x})} + \phi(\mathbf{x}), \quad (1)$$

where $\mathbf{A} \in \mathbb{C}^{ML \times N}$ refers to the forward model defining the mapping from the image \mathbf{x} to the acquired k-space data \mathbf{y} and

T. Hong is with the Department of Radiology, University of Michigan, Ann Arbor, MI 48109, USA (Email: tahong@umich.edu). TH was partly supported by National Institutes of Health grant R01NS112233.

X. Xu, J. Hu, and J. Fessler are with the Department of Electrical and Computer Engineering, University of Michigan, Ann Arbor, MI 48109, USA (Email: {xjxu, jashu, fessler}@umich.edu).

L is the number of coils. \mathbf{A} consists of a stack of matrices \mathbf{A}_l such that $\mathbf{A} = [\mathbf{A}_1; \mathbf{A}_2; \dots; \mathbf{A}_L]$ where $\mathbf{A}_l \in \mathbb{C}^{M \times N} \triangleq \mathbf{MFC}_l$. $\mathbf{M} \in \mathbb{R}^{M \times N}$ defines the sampling pattern and $\mathbf{F} \in \mathbb{C}^{N \times N}$ denotes the (non-uniform) Fourier transform operator. $\mathbf{C}_l \in \mathbb{C}^{N \times N}$ represents the sensitivity map associated with the l th coil and is patient specific.

The data-fit term $f(\cdot)$ encourages consistency of the image \mathbf{x} with the measurements \mathbf{y} and $\phi(\cdot)$ is a regularizer that describes the statistical distribution of the unknown image \mathbf{x} , often called a prior. Classical choices for $\phi(\cdot)$ that have shown to be useful for MRI reconstruction include total variation (TV) [4, 6, 7], wavelets [8, 9], dictionary learning [10, 11], and low-rank [12], to name a few. See [13, 14] for reviews of different choices of $\phi(\cdot)$. In the past decade, deep learning (DL) has gained a lot of attention in reconstructing MRI images due to its excellent performance. Instead of hand-crafting explicit priors, DL provides a data-drive tool for implicitly encoding image priors. Popular DL-based approaches for MRI reconstruction include end-to-end mapping [15] and model-based deep unrolling [16–18]. Recently, using generative models to learn a prior for solving MRI reconstruction has received extensive interest [19, 20].

Plug-and-Play (PnP) [21] is an alternative to DL that leverages the most effective image denoisers, such as BM3D [22] or DnCNN [23], leading to state-of-the-art performance in various imaging tasks [24–29]. Differing from DL approaches that usually rely on training with massive data for a predefined imaging task, PnP can be easily customized to a specific application without retraining. This feature is particularly beneficial for solving CS MRI problems, where the sampling patterns, coil sensitivity maps, and image resolution can vary significantly from scan to scan. Detailed discussions about using PnP for MRI reconstruction are found in [30].

PnP originates from the proximal algorithms [31], which is a class of iterative algorithms for solving (1). At the k th iteration, the (accelerated) proximal gradient method, which is also called (Fast) Iterative Shrinkage-Thresholding Algorithm ((F)ISTA) [32], updates the next iterate as

$$\begin{aligned} \mathbf{x}_{k+1} &\leftarrow \text{prox}_{\alpha\phi}(\mathbf{z}_k - \alpha\nabla f(\mathbf{z}_k)) \\ \mathbf{z}_{k+1} &\leftarrow \mathbf{x}_{k+1} + c_k(\mathbf{x}_{k+1} - \mathbf{x}_k), \end{aligned}$$

where $\alpha > 0$ is the step size, $c_k > 0$ encodes the acceleration mechanism, and $\nabla f(\cdot)$ denotes the gradient of $f(\cdot)$. Here, $\text{prox}_{\alpha\phi}(\cdot)$ represents the proximal operator defined as

$$\text{prox}_{\alpha\phi}(\cdot) \triangleq \underset{\mathbf{x} \in \mathbb{C}^N}{\text{argmin}} \frac{1}{2} \|\mathbf{x} - \cdot\|_2^2 + \alpha\phi(\mathbf{x}). \quad (2)$$

The observation that (2) can be interpreted as a denoiser inspired the development of PnP-(F)ISTA algorithm, where the proximal operator is replaced with an arbitrary denoiser $D_\sigma(\cdot)$. Here, σ^2 represents the variance of the additive white Gaussian noise and is related to the strength of the regularizer, e.g., a large σ means more regularization. In PnP practice, the value of σ is often selected via empirical parameter tuning, after choosing the step size α based on a Lipschitz constant for ∇f . PnP-ADMM [33] is another popular PnP approach that comes from the Alternating Direction Method of Multipliers (ADMM) [34]. Section II discusses PnP approaches and their convergence properties.

Despite the rich literature that elaborate on the benefits of using PnP for image reconstruction, efficiently solving PnP optimization problems remains computationally challenging, particularly for multi-coils non-Cartesian sampling CS MRI reconstruction. Frequent use of the forward model \mathbf{A} results in significant computational expense in CS MRI reconstruction. This work focuses on this challenge and proposes a *Preconditioned* PnP (P^2 nP) method to accelerate the convergence speed of PnP-(F)ISTA algorithm. The main *contributions* of our work are summarized as follows:

- 1) We proposed a new preconditioned solver for PnP called P^2 nP that improves the convergence speed of PnP-(F)ISTA algorithm. In particular, we presented two different strategies for designing the preconditioners, i.e., *fixed* and *dynamic*, where the fixed one is pre-determined using the forward model \mathbf{A} , and the dynamic one is estimated at each iteration with negligible cost. Since the estimation of the dynamical preconditioner does not rely on the evaluation of \mathbf{A} , it is especially useful when computing $\mathbf{A}\mathbf{x}$ is computationally expensive.
- 2) We established the theoretical convergence and stability analysis of P^2 nP. Our proofs showed that, under mild conditions, P^2 nP achieves the fixed-point convergence for both *fixed* and the *dynamic* preconditioners.
- 3) We applied *normalization-equivariant* denoisers in the PnP framework. Our results demonstrated that, compared with ordinary CNN denoisers, noise-adapted and robust normalization-equivariant denoisers can effectively boost the performance of PnP, compared to existing PnP methods for which the selection of denoising strength is tricky.
- 4) We extensively tested P^2 nP for multi-coils non-Cartesian sampling CS MRI reconstruction in a variety of settings, including with fixed and dynamic preconditioners, spiral and radial sampling trajectories, and a normalization-equivariant denoiser. Our numerical results showed that P^2 nP consistently outperforms the baseline methods regarding not only the convergence speed but also the reconstruction performance, both qualitatively and quantitatively.

The rest of the paper is organized as follows. Section II presents some popular existing variants and convergence properties of PnP. Section III proposes our preconditioned PnP (P^2 nP) method and discusses the convergence properties of P^2 nP. Section IV summarizes the experimental validation of P^2 nP for CS MRI reconstruction and the comparison with other known baseline methods. Furthermore, we examine

the convergence of P^2 nP to verify our theoretical analyses. Section V concludes the paper.

II. PRELIMINARIES ON PnP APPROACHES

This section reviews different variants of PnP and their convergence properties. PnP is a family of imaging algorithms that interpret the prior with a black-box denoiser. For example, beyond PnP-ADMM and PnP-(F)ISTA, PnP can be developed from other algorithms, such as PnP-PDS [25], PnP-HQS [35], and PnP-CE [27], etc. An alternative to PnP is regularization by denoising (RED) [36–38] that forms an explicit denoiser-embedded regularization function. To accelerate the convergence of PnP, Tan et al. [39] proposed a PnP-quasi-Newton approach incorporating quasi-Newton steps into a provable PnP framework. However, their method is quite complicated and the computation at each step is very expensive. Pendu et al. [40] showed a preconditioned PnP-ADMM algorithm but the preconditioner is a diagonal matrix that is ineffective for many applications. Moreover, it is nontrivial to find such a preconditioner when the explicit formulation of \mathbf{A} is unknown.

Besides the empirical success of PnP, the convergence analyses of PnP also has made much progress. In [24], Sreehari et al. provided sufficient conditions for the convergence of PnP with respect to some implicit objective function. Chan et al. [33] established the fixed-point convergence of PnP-ADMM for bounded denoisers. Buzzard et al. [27] proposed a fixed-point interpretation of PnP from the consensus equilibrium view. Teodoro et al. [41] established the convergence for PnP-ADMM with linearized Gaussian mixture model denoisers. Gavaskar et al. [42] showed the convergence of PnP with an explicit cost function for linear denoisers. Recent analysis showed that the convergence of PnP iterates can also be ensured under other assumptions about the denoisers [43–48]. Related work on RED convergence analysis includes [36, 38, 49]. See [50] and the references therein for detailed discussions of PnP convergence properties.

III. PROPOSED METHOD

This section first presents our P^2 nP method and then describes two different strategies for choosing the preconditioner: fixed and dynamic. We also provide the convergence and stability analyses for P^2 nP.

Let $\mathbf{P} \succ \mathbf{0}$ denote a Hermitian positive matrix in $\mathbb{C}^{N \times N}$. At the k th iteration, P^2 nP solves the following problem:

$$\begin{aligned} \mathbf{x}_{k+1} &= \underset{\mathbf{u} \in \mathbb{C}^N}{\operatorname{argmin}} \left\{ \langle \nabla f(\mathbf{x}_k), \mathbf{u} - \mathbf{x}_k \rangle \right. \\ &\quad \left. + \frac{1}{2\alpha} (\mathbf{u} - \mathbf{x}_k)^{\mathcal{H}} \mathbf{P}^{-1} (\mathbf{u} - \mathbf{x}_k) + \phi(\mathbf{u}) \right\} \\ &= \underset{\mathbf{u} \in \mathbb{C}^N}{\operatorname{argmin}} \left\{ \frac{1}{2} \|\mathbf{u} - (\mathbf{x}_k - \alpha \mathbf{P} \nabla f(\mathbf{x}_k))\|_{\mathbf{P}^{-1}}^2 \right. \\ &\quad \left. + \alpha \phi(\mathbf{u}) \right\}, \end{aligned} \quad (3)$$

where α is the step-size, \mathcal{H} denotes the Hermitian transpose, and we define the weighted Euclidean norm $\|\mathbf{v}\|_{\mathbf{P}^{-1}}^2 \triangleq \mathbf{v}^{\mathcal{H}} \mathbf{P}^{-1} \mathbf{v}$. Clearly, if $\mathbf{P} = \mathbf{I}$, then P^2 nP reverts to PnP-ISTA.

Algorithm 1 Preconditioned Plug-and-Play (P²nP)**Initialization:** \mathbf{x}_1 and step-size $\alpha > 0$.**Iteration:**

- 1: **for** $k = 1, 2, \dots$ **do**
- 2: $\mathbf{x}_{k+1} \leftarrow \mathbf{D}_\sigma(\mathbf{x}_k - \alpha \mathbf{P} \nabla f(\mathbf{x}_k))$.
- 3: **end for**

Using the fact that $\|\mathbf{v}\|_{\mathbf{P}^{-1}}^2 \leq \|\mathbf{P}^{-1}\|_2 \|\mathbf{v}\|_2^2$, we remove the weighting \mathbf{P}^{-1} in (3) by using the update

$$\mathbf{x}_{k+1} = \operatorname{argmin}_{\mathbf{u} \in \mathbb{C}^N} \frac{1}{2} \|\mathbf{u} - (\mathbf{x}_k - \alpha \mathbf{P} \nabla f(\mathbf{x}_k))\|_2^2 + \frac{\alpha}{\eta} \phi(\mathbf{u}), \quad (4)$$

where $\eta \triangleq \|\mathbf{P}^{-1}\|_2 > 0$. Aminifard et al. [51] proved that convergence of the function value sequence $\{f(\mathbf{x}_k)\}$ in (1) is still guaranteed when solving (4) instead of (3) with an extra line search step. The following section shows a stronger result, namely that convergence of the iterates sequence $\{\mathbf{x}_k\}$ of P²nP still holds under mild assumptions even without an extra line search step.

Clearly, (4) is very similar to the definition of the proximal operator in (2). So we replace this proximal operator with a denoiser \mathbf{D}_σ , leading to our proposed P²nP algorithm summarized in Algorithm 1. One can treat $\frac{1}{\eta}$ in (4) as a trade-off parameter. When $\frac{1}{\eta} > 1$, we should emphasize $\phi(\mathbf{u})$ more, so the denoiser should use a larger σ value than the one used for (2). For a given choice of \mathbf{P} and step size α , one can fine-tune an appropriate σ value empirically in light of (4).

Similar to PnP-FISTA, one could try to accelerate P²nP using momentum. However, we experimentally found that the performance of *both* PnP-FISTA and the accelerated P²nP degraded significantly after running ‘‘too many’’ iterations, a problem needing further investigation in the future. So this paper focuses on Algorithm 1. Next we show two different ways to choose the preconditioner \mathbf{P} .

A. Fixed Preconditioners

We first discuss the convergence of P²nP to gain insights into the kinds of preconditioners \mathbf{P} that can improve the convergence rate and then show how to choose a fixed \mathbf{P} efficiently in practice.

1) *Convergence Analysis:* Here we discuss the convergence condition of P²nP and its convergence rate bound. First, we assume the denoiser is Lipschitz continuous, a standard assumption in the analysis of fixed-point PnP [44], i.e., Assumption 1.

Assumption 1. *The denoiser $\mathbf{D}_\sigma(\cdot) : \mathbb{C}^N \rightarrow \mathbb{C}^N$ is Lipschitz continuous with Lipschitz constant $1 + \epsilon$ for $\epsilon > 0$ so that the following inequality is satisfied for all $\mathbf{x}, \mathbf{y} \in \mathbb{C}^N$,*

$$\|\mathbf{D}_\sigma(\mathbf{x}) - \mathbf{D}_\sigma(\mathbf{y})\| \leq (1 + \epsilon) \|\mathbf{x} - \mathbf{y}\|.$$

Then Theorem 1 provides a sufficient condition for convergence of the P²nP iterates to a fixed-point.

Theorem 1 (Convergence of P²nP with fixed preconditioner). *Assume $\mathbf{D}_\sigma(\cdot)$ satisfies Assumption 1. Then the iterates se-*

quence generated by Algorithm 1 converges to a fixed-point if

$$r_0 \triangleq (1 + \epsilon) \rho(\mathbf{I} - \alpha \mathbf{P} \mathbf{A}^H \mathbf{A}) < 1, \quad (5)$$

where $\rho(\cdot)$ denotes the spectral radius, and the convergence rate of the iterates is upper bounded by that r_0 .

See Appendix A for the proof.

From Theorem 1, an ideal $\alpha \mathbf{P}$ should be chosen to minimize $\rho(\mathbf{I} - \alpha \mathbf{P} \mathbf{A}^H \mathbf{A})$. If $\mathbf{A}^H \mathbf{A} \succ 0$, the ideal choice would be $\alpha \mathbf{P} = (\mathbf{A}^H \mathbf{A})^{-1}$ so that Algorithm 1 would converge to a fixed-point in one iteration. However, the computation of such an $\alpha \mathbf{P}$ is expensive, and, in CS MRI, $\mathbf{A}^H \mathbf{A}$ is a Hermitian positive semi-definite matrix, so choosing such an $\alpha \mathbf{P}$ is impractical.

2) *The Choice of Preconditioners $\alpha \mathbf{P}$:* Finding a $\alpha \mathbf{P}$ to minimize $\rho(\mathbf{I} - \alpha \mathbf{P} \mathbf{A}^H \mathbf{A})$ is a non-trivial task. One approach that has proved to be useful in the scientific computing community is to minimize an upper bound of $\rho(\mathbf{I} - \alpha \mathbf{P} \mathbf{A}^H \mathbf{A})$ [52, 53], i.e.,

$$\min_{\alpha \mathbf{P}} \|\mathbf{I} - \alpha \mathbf{P} \mathbf{A}^H \mathbf{A}\|_F^2. \quad (6)$$

In CS MRI, we do not store dense matrix \mathbf{A} explicitly, so using (6) would be challenging. Moreover, \mathbf{A} is different for each scan because of the patient-dependent coil sensitivity maps, making any expensive pre-computing strategies impractical.

In this paper, we suggest using polynomial preconditioners of the following form [54]:

$$\mathbf{P} = \sum_{\gamma=1}^{\Gamma} p_\gamma (\alpha \mathbf{A}^H \mathbf{A})^{\gamma-1},$$

where the cost of finding $\{p_\gamma\}_\gamma$ for an effective \mathbf{P} is negligible. For instance, Zulfiqar et al. in [55] set

$$p_\gamma = \binom{\Gamma}{\gamma} (-1)^{\gamma-1}, \quad (7)$$

and showed its effectiveness for wavelet-based image reconstruction.

An alternative approach is used in [56], where Iyer et al. showed the effectiveness of Chebyshev polynomial preconditioners for CS MRI reconstruction with low-rank regularization. Because $\mathbf{A}^H \mathbf{A}$ is Hermitian, all its eigenvalues are real, allowing the use of Chebyshev polynomial preconditioners that are optimal for minimizing $\rho(\mathbf{I} - \alpha \mathbf{P} \mathbf{A}^H \mathbf{A})$. By finding the smallest and largest eigenvalue of $\mathbf{A}^H \mathbf{A}$, we can get the values of $\{p_\gamma\}_\gamma$ analytically. In CS MRI, \mathbf{A} is usually under-determined, so the smallest eigenvalue of $\mathbf{A}^H \mathbf{A}$ is zero and we obtain the largest eigenvalue by the power method.

By using a recursive implementation, applying $\mathbf{P} \mathbf{x}$ needs to compute $\mathbf{A}^H \mathbf{A} \mathbf{x}$ a total of $(\Gamma - 1)$ times. In modern CS MRI, performing $\mathbf{A}^H \mathbf{A} \mathbf{x}$ is also expensive due to the use of multi-coils and non-Cartesian acquisition, so a large Γ can dramatically increase computational costs. Hence, in this paper, we used $\Gamma = 2$. To further reduce the computation in the polynomial preconditioners, we study dynamic preconditioners in the next part, where the additional computation at each iteration is negligible.

B. Dynamic Preconditioners

Theorem 1 indicates that a well-designed preconditioner should approximate the inverse of $\mathbf{A}^H \mathbf{A}$. So an alternative approach is to use quasi-Newton methods [57, Ch. 6] to define a \mathbf{P} that approximates $(\mathbf{A}^H \mathbf{A})^{-1}$. Following [58–60], we suggest using the zero-memory self-scaling Hermitian rank-1 (ZMSHR1) for complex data to define such a preconditioner. Algorithm 2 summarizes the ZMSHR1 approach. Since (9) is a one-dimensional minimization problem, we simply search for the minimal a . Lemma 1 specifies some properties of the variables generated by Algorithm 2.

Lemma 1. *Suppose $f(\mathbf{x}) = \frac{1}{2} \|\mathbf{A}\mathbf{x} - \mathbf{y}\|_2^2$ with $\mathbf{x} \in \mathbb{C}^N$. Then τ_k and $\langle \mathbf{s}_k, \mathbf{v}_k \rangle$ generated in Algorithm 2 are real and $\langle \mathbf{s}_k - \tau_k \mathbf{v}_k, \mathbf{v}_k \rangle \geq 0$. Moreover, the generated τ_k and $\mathbf{P}_k \in \mathbb{C}^{N \times N}$ for $\forall k$ are bounded by*

$$\begin{aligned} \frac{1}{2\theta_2} < \tau_k &\leq \frac{1}{\theta_1}, \\ \frac{1}{2\theta_2} \preceq \mathbf{P}_k &\preceq \frac{\delta+1}{\delta\theta_1}, \end{aligned}$$

where $\delta > 0$, $\theta_1 \in (0, 1)$, and $\theta_2 \in (1, \infty)$.

See Appendix B for the proof.

Lemma 1, ensures that \mathbf{P}_k is a positive-definite matrix. Let $\eta_k \triangleq \|\mathbf{P}_k^{-1}\|_2$. Then, at the k th iteration, the dynamic preconditioner version of P^2nP solves the following problem instead of (4):

$$\mathbf{x}_{k+1} = \underset{\mathbf{u} \in \mathbb{C}^N}{\operatorname{argmin}} \frac{1}{2} \|\mathbf{u} - (\mathbf{x}_k - \alpha \mathbf{P}_k \nabla f(\mathbf{x}_k))\|_2^2 + \frac{\alpha}{\eta_k} \phi(\mathbf{u}). \quad (8)$$

Clearly, η_k differs at each iteration, so solving (8) is not equivalent to executing a denoiser with a fixed σ for all iterations. In [61], Xu et al. proved that if $\mathbf{D}_\sigma(\cdot)$ denotes a minimum mean-squared error (MMSE) denoiser for image data with noise standard deviation σ , then $\frac{1}{\mu} \mathbf{D}_\sigma(\mu \mathbf{x})$, $\mu > 0$ is the MMSE denoiser for an image with noise level σ^2/μ^2 . Moreover, Xu et al. [47] showed many modern denoisers like BM3D [22] and trained CNN denoisers can be treated experimentally as MMSE denoisers. So, for a given η_k , one could, in principle, solve (8) by (somehow) finding a suitable η_k^* and running $\frac{1}{\eta_k^*} \mathbf{D}_\sigma(\eta_k^* \mathbf{x})$ if $\mathbf{D}_\sigma(\cdot)$ is a MMSE denoiser. However, finding η_k^* in practice is a nontrivial task.

Herbreteau et al. in [62] proposed a normalization-equivariant CNN denoiser that performs as well as an ordinary denoiser and can denoise noisy images across various noise levels. Specifically, the normalization-equivariant denoiser has a special property that, for any $\mu \in \mathbb{R}$ with $\mu > 0$ and $\Delta \in \mathbb{C}$, we have $\mathbf{D}_\sigma(\mu \mathbf{x} + \Delta \mathbf{1}) = \mu \mathbf{D}_\sigma(\mathbf{x}) + \Delta \mathbf{1}$, where $\mathbf{1}$ denotes the vector of ones. By using the normalization-equivariant denoiser, we can simply apply $\mathbf{D}_\sigma(\mathbf{x}_k - \alpha \mathbf{P}_k \nabla f(\mathbf{x}_k))$ instead of (8) without needing to adjust the associated noise level σ for different η_k values; this property makes using a dynamic preconditioner as practical as the fixed preconditioner case. Algorithm 3 summarizes P^2nP with dynamic preconditioners.

Section IV-D compares the performance between normalization-equivariant and ordinary denoisers and shows that the normalization-equivariant denoiser outperformed the ordinary denoiser. Next, we discuss the stability property

Algorithm 2 Zero-memory self-scaling Hermitian rank-1 (ZMSHR1)

Initialization: \mathbf{x}_{k-1} , \mathbf{x}_k , $\nabla f(\mathbf{x}_{k-1})$, $\nabla f(\mathbf{x}_k)$, $\delta > 0$, $\theta_1 \in (0, 1)$, and $\theta_2 \in (1, \infty)$.

- 1: Set $\mathbf{s}_k \leftarrow \mathbf{x}_k - \mathbf{x}_{k-1}$ and $\mathbf{m}_k \leftarrow \nabla f(\mathbf{x}_k) - \nabla f(\mathbf{x}_{k-1})$.
- 2: Compute α such that

$$\begin{aligned} \min_a \{a \in [0, 1] \mid \mathbf{v}_k = a \mathbf{s}_k + (1-a) \mathbf{m}_k\} \\ \text{satisfies } \theta_1 \leq \frac{\langle \mathbf{s}_k, \mathbf{v}_k \rangle}{\langle \mathbf{s}_k, \mathbf{s}_k \rangle} \text{ and } \frac{\langle \mathbf{v}_k, \mathbf{v}_k \rangle}{\langle \mathbf{s}_k, \mathbf{v}_k \rangle} \leq \theta_2. \end{aligned} \quad (9)$$

- 3: Compute $\tau_k \leftarrow \frac{\langle \mathbf{s}_k, \mathbf{s}_k \rangle}{\langle \mathbf{s}_k, \mathbf{v}_k \rangle} - \sqrt{\left(\frac{\langle \mathbf{s}_k, \mathbf{s}_k \rangle}{\langle \mathbf{s}_k, \mathbf{v}_k \rangle}\right)^2 - \frac{\langle \mathbf{s}_k, \mathbf{s}_k \rangle}{\langle \mathbf{v}_k, \mathbf{v}_k \rangle}}$.

- 4: **if** $\langle \mathbf{s}_k - \tau_k \mathbf{v}_k, \mathbf{v}_k \rangle \leq \delta \|\mathbf{s}_k - \tau \mathbf{v}_k\| \|\mathbf{v}_k\|$ **then**

- 5: $\mathbf{u}_k \leftarrow \mathbf{0}$.

- 6: **else**

- 7: $\mathbf{u}_k \leftarrow \mathbf{s}_k - \tau_k \mathbf{v}_k$.

- 8: **end if**

- 9: **Return:** $\mathbf{P}_k \leftarrow \tau_k \mathbf{I} + \frac{\mathbf{u}_k \mathbf{u}_k^H}{\langle \mathbf{s}_k - \tau \mathbf{v}_k, \mathbf{v}_k \rangle}$.
-

Algorithm 3 P^2nP with dynamic preconditioners

Initialization: \mathbf{x}_1 , step-size $\alpha \in \mathbb{R}$,

and $\mathbf{D}_\sigma(\cdot)$ is a normalization-equivariant denoiser.

Iteration:

- 1: **for** $k = 1, 2, \dots$ **do**

- 2: **if** $k=1$ **then**

- 3: $\mathbf{x}_{k+1} \leftarrow \mathbf{D}_\sigma(\mathbf{x}_k - \alpha \nabla f(\mathbf{x}_k))$.

- 4: **else**

- 5: Call Algorithm 2 to get \mathbf{P}_k .

- 6: $\mathbf{x}_{k+1} \leftarrow \mathbf{D}_\sigma(\mathbf{x}_k - \alpha \mathbf{P}_k \nabla f(\mathbf{x}_k))$.

- 7: **end if**

- 8: **end for**
-

of Algorithm 3, ensuring that the iterates \mathbf{x}_k generated by Algorithm 3 will always be close to a fixed-point.

1) *Stability Analysis:* In this part, we present the stability analysis of P^2nP when using dynamic preconditioners. We show that Algorithm 3 is reliable in the sense that the iterates \mathbf{x}_k remain in a bounded set. We first assume the gradient of f is upper bounded.

Assumption 2. *For $\forall \mathbf{x}_k$ generated by Algorithm 3, there exists $R < \infty$ such that*

$$\|\nabla f(\mathbf{x}_k)\| \leq R.$$

Note that the bound R exists in practice since many denoising algorithms have bounded range spaces [45] and $\nabla f(\mathbf{x}) = \mathbf{A}^H(\mathbf{A}\mathbf{x} - \mathbf{y})$. Theorem 2 defines an upper bound on $\|\mathbf{x}_k - \mathbf{x}_*\|$.

Theorem 2 (Stability of Algorithm 3). *Suppose a Hermitian positive matrix \mathbf{P}_* satisfies $\mathbf{0} \prec \mathbf{P}_* \preceq \lambda_* \mathbf{I}$ with $\lambda_* < \infty$, and $q \triangleq [(1 + \epsilon) \rho(\mathbf{I} - \alpha \mathbf{P}_* \mathbf{A}^H \mathbf{A})] < 1$. Let $\{\mathbf{P}_k\}_k$ denote the dynamic preconditioners generated by Algorithm 2 and assume a normalization-equivariant denoiser is used. Then $\|\mathbf{x}_k - \mathbf{x}_*\|$ with \mathbf{x}_k generated by Algorithm 3 and $\mathbf{x}_* \triangleq$*

$D_\sigma(\mathbf{x}_* - \alpha \mathbf{P}_* \nabla f(\mathbf{x}_*))$ is upper bounded by

$$\|\mathbf{x}_{k+1} - \mathbf{x}_*\| \leq q^k \|\mathbf{x}_1 - \mathbf{x}_*\| + \frac{(1 + \epsilon)\alpha(\delta + 1 + \delta\theta_1\lambda_*)}{\delta\theta_1(1 - q)} R. \quad (10)$$

See Appendix C for the proof.

Since $q < 1$, when $k \rightarrow \infty$, the first term in (10) will vanish and the distance $\|\mathbf{x}_k - \mathbf{x}_*\|$ is controlled by the second term. In our experiments, we found $R = \|\nabla f(\mathbf{x}_1)\|$, so a good initial value with small $\|\nabla f(\mathbf{x}_1)\|$ can help to control the error. Moreover, one can control the accuracy of the error bound by setting other parameters to a desired level. However, we experimentally identified that the excellent PSNR performance of Algorithm 3 can be achieved without tuning the value of the second term in (10), coinciding with the observation in [45, Thm. 1].

IV. NUMERICAL EXPERIMENTS

This section studies the performance of P²nP with fixed and dynamic preconditioners for CS MRI reconstruction with spiral and radial sampling trajectories. For the fixed preconditioners, we examined (7) and the Chebyshev polynomials, and investigate the convergence of P²nP to verify our analyses. Lastly, we compared the performance of normalization-equivariant and ordinary denoisers. We first present our experimental and algorithmic settings and then show the reconstruction results.

Experimental Settings: The brain and knee MRI images were used to study the performance of P²nP. For the brain images, we adopted the dataset used in [16] that has 360 images in the training dataset and 164 images in the testing dataset. For the knee images, we used the NYU fastMRI [63] multi-coil knee dataset, where we first applied the ESPiRiT algorithm [64] to recover the complex-valued images and then took 700 and 6 slices from the training and testing datasets, respectively. We then cropped and resized all brain and knee images to 256×256 . For the denoiser, we used the DRUNet [29] and trained both normalization-equivariant [62] and ordinary denoisers for brain and knee images.

We took six images from the brain and knee testing datasets as the ground truth and scaled the maximum magnitude of images to be one. Figure 1 shows the magnitude of the six complex-valued ground truth images. For the sampling trajectories, we used 6 interleaves, 1688 readout points, and 32 coils (respectively, 21 spokes with golden angle rotation, 1024 readout points, and 32 coils) for the spiral (respectively, radial) trajectory to specify the forward model \mathbf{A} . Figure 2 illustrates the trajectories used in this paper. We applied the related forward models to the ground truth images to generate the noiseless multi-coil k-space data and then added complex i.i.d Gaussian noise with mean zero and variance 10^{-3} (respectively, 3×10^{-4}) to all coils for the brain (respectively, knee) images to form the associated measurements \mathbf{y} . Sections IV-C and IV-D examine the whole six brain test images with the spiral acquisition. All experiments were implemented in PyTorch [65] and run on NVIDIA GeForce RTX 3090.

Algorithmic Settings: The step-size α was set to be $1/\|\mathbf{A}^H \mathbf{A}\|_2$, where the spectral norm was computed by the

power method. For P²nP with fixed preconditioners, we studied two different strategies: one with $\Gamma = 2$ such that $\mathbf{P}_1^F = 2 - \alpha \mathbf{A}^H \mathbf{A}$ through (7) dubbed ‘‘P²nP-F-1’’, and the other with $\mathbf{P}_2^F = 4 - \frac{10}{3} \alpha \mathbf{A}^H \mathbf{A}$ through the Chebyshev polynomials dubbed ‘‘P²nP-F-Cheb’’. P²nP with dynamic preconditioner is denoted by ‘‘P²nP-D’’. Algorithm 2 used $\delta = 10^{-8}$, $\theta_1 = 2 \times 10^{-6}$, $\theta_2 = 200$. We mainly compared P²nP with PnP-ISTA and PnP-ADMM methods [33, 44] since those methods also have provable fixed-point convergence under mild assumptions. All algorithms in this paper were run for 200 iterations except in Section IV-C, where we ran 500 iterations to examine the convergence properties. Moreover, we used the normalization-equivariant denoiser in all the experiments except in Section IV-D, where we compared the difference between normalization-equivariant and ordinary denoisers.

A. Spiral Acquisition Reconstruction

Figure 3 presents the performance of P²nP for the brain 1 image. Figure 3(a) shows that P²nP with fixed and dynamic preconditioners converged faster than PnP-ISTA and PnP-ADMM in terms of iteration number, demonstrating the effectiveness of using preconditioners and the fastest convergence speed of Algorithm 3. Moreover, P²nP-F-Cheb was faster than P²nP-F-1, coinciding with our expectation since P²nP-F-Cheb is optimal. Figure 3(b) displays the PSNR values versus wall time. P²nP-D was the most appealing algorithm in this experiment because it converged faster (both in terms of iterations run and walltime) than the other algorithms. Figure 3(b) shows that P²nP-F-1 and P²nP-F-Cheb needed almost twice as much wall time as ISTA. This was because P²nP-F-1 and P²nP-F-Cheb executed $\mathbf{A}\mathbf{x}$ twice as often as PnP-ISTA. Nevertheless, P²nP-F-1 and P²nP-F-Cheb still converged faster than PnP-ISTA in terms of wall time. PnP-ADMM was the slowest algorithm across all methods in terms of wall time because ADMM needed to solve a least-squares problem at each iteration, requiring executing $\mathbf{A}\mathbf{x}$ many times. Figure 4 depicts the reconstructed images at the 25, 50, 100, and 200th iterations and the associated error maps at the 200th iteration and shows that P²nP achieved a higher PSNR and clearer image reconstruction than PnP-ISTA with the same number of iterations.

Table I presents the performance of different methods for the reconstruction of other brain test images, where we used the highest PSNR obtained by PnP-ADMM as a benchmark. Firstly, PnP-ISTA had similar PSNR as PnP-ADMM. Secondly, from the first row of each method in Table I, P²nP took fewer iterations and less wall time than PnP-ISTA and PnP-ADMM, to reach a similar PSNR. This consistent advantage of P²nP demonstrates the effectiveness of using preconditioners. Moreover, P²nP-D was almost 70 times faster than PnP-ADMM and $7 \sim 10$ times faster than PnP-ISTA to reach a similar PSNR, illustrating the advantages and efficiency of using dynamic preconditioners. The second row of each method in Table I indicated that P²nP-D also yielded the highest PSNR after running all scheduled iterations. Overall, in this experiment, P²nP-D was the fastest algorithm in terms of

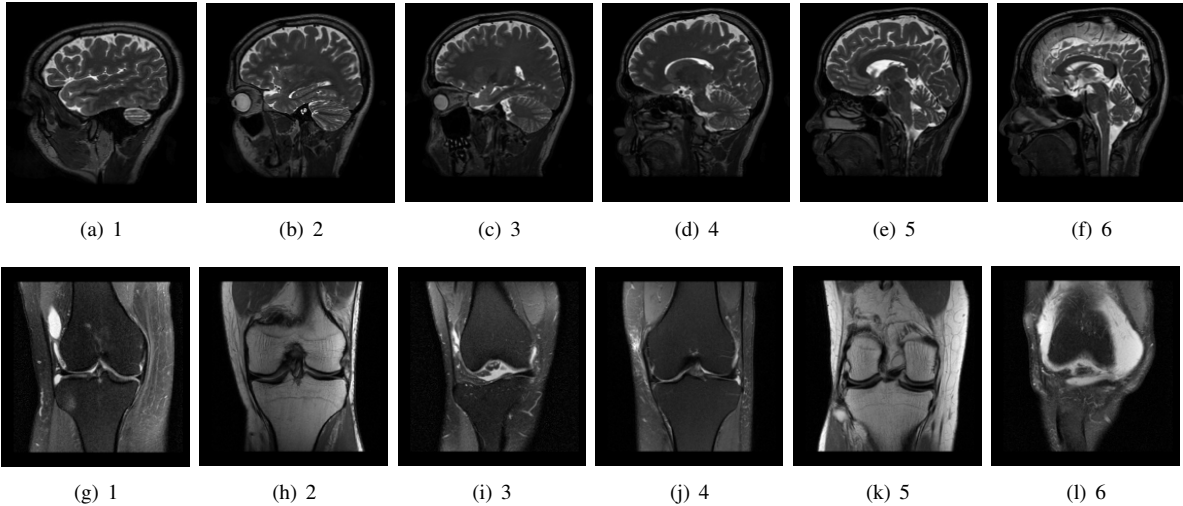


Fig. 1. The magnitude of the six brain and knee complex-valued ground truth images.

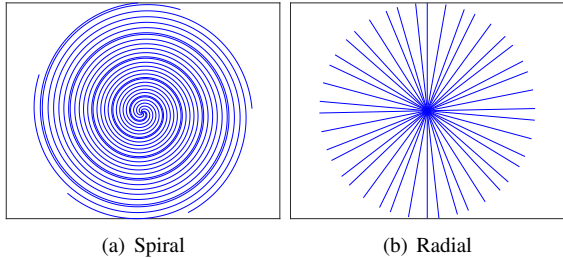


Fig. 2. The non-Cartesian k-space sampling trajectories used in this paper.

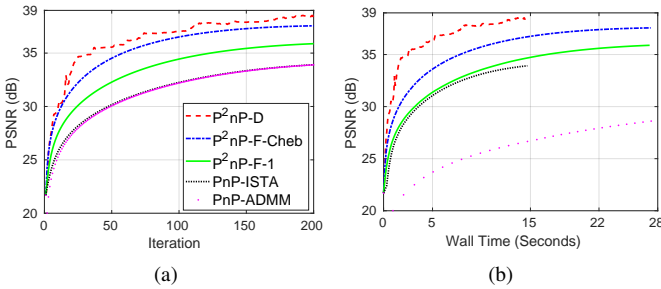


Fig. 3. PSNR values versus iteration and wall (GPU) time on the brain 1 image with spiral acquisition.

iteration and wall time. The supplementary material provides the results of knee images with spiral acquisition where we observed similar trends as the brain images.

B. Radial Acquisition Reconstruction

Figure 5 describes the performance of different methods for the reconstruction of knee 1 image. Consistent with the observations in the brain-image-based experiments in Section IV-A, P^2nP converged faster than PnP-ADMM and PnP-ISTA in terms of iteration and wall time. Additionally, in this experiment, P^2nP -D converged at a rate similar to P^2nP -F-Cheb in terms of iterations run but P^2nP -D was faster than P^2nP -F-Cheb in terms of wall time. Although the PSNR value of P^2nP -F-Cheb dropped slightly at the end of the iterations, it

was still faster than P^2nP -F-1. Similar to Section IV-A, P^2nP -D was the fastest algorithm. Figure 6 shows the reconstructed images for different methods. Here the reconstructed images had some aliasing artifacts because we only used 21 spokes. The supplementary material shows the reconstruction of knee 1 image with a spiral acquisition that yields much clearer reconstructed images. Moreover, we also tested on the radial acquisition with 55 spokes and the results are summarized in the supplementary material where we saw the artifacts were significantly reduced.

Similar to Table I, we also tested the other knee images and Table II summarizes the results. Here, PnP-ISTA had very slightly worse PSNR than PnP-ADMM for some test images. Moreover, for some images (i.e., 5 and 6), PnP-ISTA images has slightly lower PSNR towards the end of the iterations. This is expected because fixed-point convergence cannot guarantee the quality of the reconstructed image. Similar to Section IV-A, P^2nP was faster than PnP-ISTA and PnP-ADMM, and P^2nP -D was the fastest algorithm to exceed the performance of ADMM. However, for some images (i.e., 2, 3, 4), P^2nP -F-Cheb achieved the highest PSNR. The supplement summarizes the results of brain images with radial acquisition which showed similar trends.

C. Convergence Validation

This part studied the convergence of P^2nP . Denote by $E(\mathbf{x}_k) = \|\mathbf{x}_k - \mathbf{D}_\sigma(\mathbf{x}_k - aP\nabla f(\mathbf{x}_k))\|_2^2 / \|\mathbf{x}_1\|_2^2$, so $E(\mathbf{x}_k) \rightarrow 0$ if $\mathbf{x}_k \rightarrow \mathbf{x}_*$ where \mathbf{x}_* represents the fixed-point. Figure 7(a) shows the value of $E(\mathbf{x}_k)$ versus iteration for PnP-ISTA, P^2nP -F-1, and P^2nP -F-Cheb. We saw that $E(\mathbf{x}_k) \rightarrow 0$ for all tested methods and P^2nP converged faster than PnP-ISTA. Moreover, we noticed that the shaded region was very small, indicating that the convergence properties were similar across different test images. Figure 7(b) presents the value of $\|\nabla f(\mathbf{x}_k)\|_2^2 / \|\mathbf{x}_1\|_2^2$ for P^2nP -D. It can be seen that $\|\nabla f(\mathbf{x}_k)\|_2^2 / \|\mathbf{x}_1\|_2^2$ attained its maximal value at the first iteration and tended to zero, indicating $R = \|\nabla f(\mathbf{x}_1)\|$.

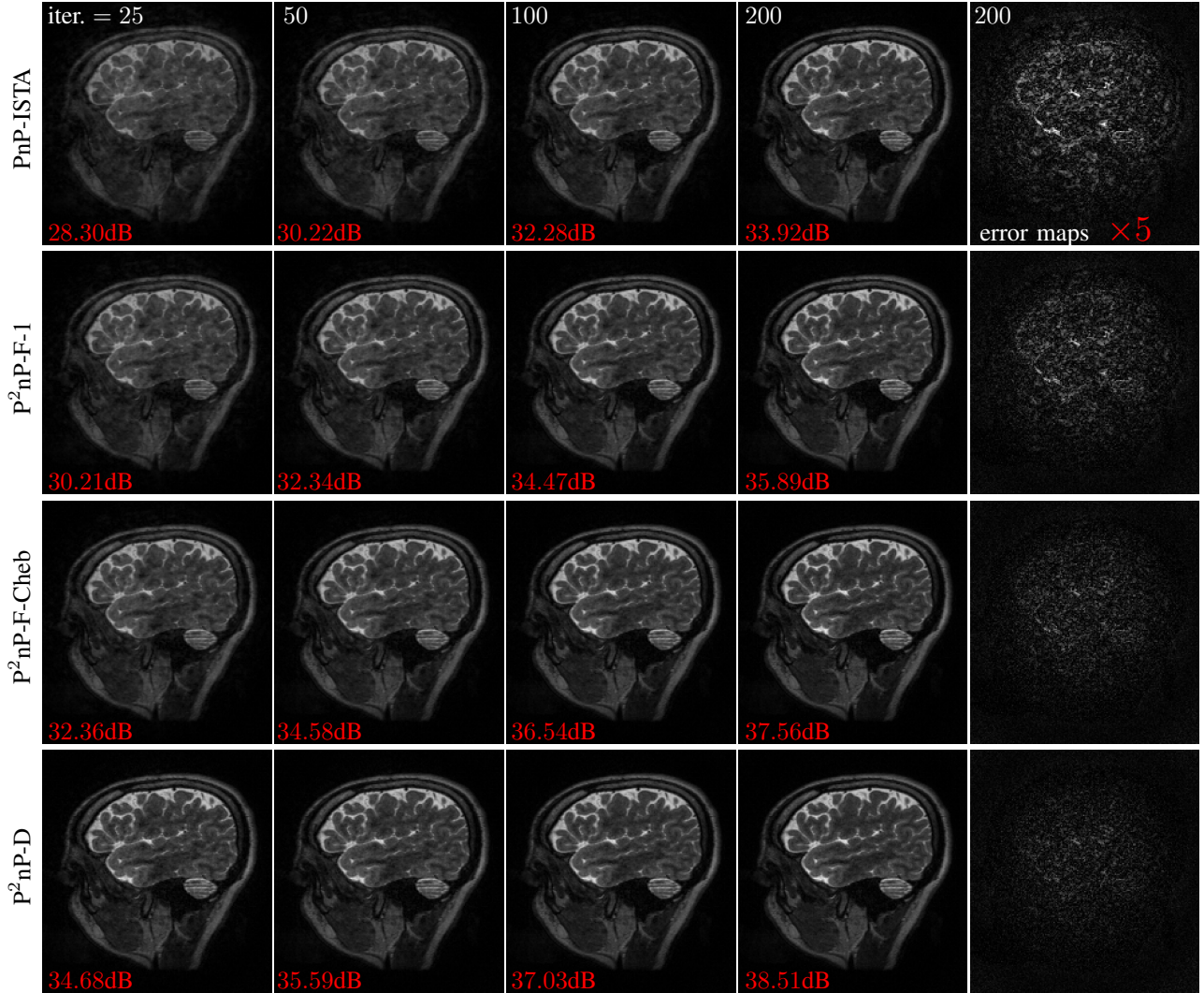


Fig. 4. The reconstructed brain 1 images at 25, 50, 100, 200th iteration with spiral acquisition. The PSNR value is labeled in the left bottom corner of each image. The fifth column shown the error maps ($\times 5$) of the reconstructed images at 200th iteration. We omitted the PnP-ADMM results since it is similar to PnP-ISTA.

TABLE I

PSNR PERFORMANCE OF EACH METHOD FOR RECONSTRUCTING 5 OTHER BRAIN TEST IMAGES WITH SPIRAL ACQUISITION. FOR PnP-ADMM, WE SHOWED THE MAXIMAL PSNR AND THE ASSOCIATED NUMBER OF ITERATIONS, AND WALL TIME THAT IS USED AS THE BENCHMARK. FOR OTHER METHODS ON EACH TEST IMAGE, THE SECOND COLUMN OF THE FIRST ROW REPRESENTS THE FIRST ITERATION THAT EXCEEDED PnP-ADMM PSNR. THE RELATED FIRST AND THIRD COLUMNS ARE THE ASSOCIATED PSNR AND WALL TIME, RESPECTIVELY. THE **BOLD** DIGITS DENOTE THE NUMBER OF ITERATIONS AND WALL TIME OF THE FASTEST ALGORITHM THAT FIRST EXCEEDED PnP-ADMM. THE SECOND ROW SHOWS THE PSNR AND WALL TIME AT THE 200TH ITERATION. THE **BLUE** DIGITS DENOTE THE HIGHEST PSNR AT THE 200TH ITERATION.

Methods \ Index	2			3			4			5			6		
	PSNR \uparrow	iter. \downarrow	sec. \downarrow	PSNR \uparrow	iter. \downarrow	sec. \downarrow	PSNR \uparrow	iter. \downarrow	sec. \downarrow	PSNR \uparrow	iter. \downarrow	sec. \downarrow	PSNR \uparrow	iter. \downarrow	sec. \downarrow
PnP-ADMM	34.29	200	147.6	34.51	200	152.2	34.09	200	149.3	32.78	200	148.7	31.70	200	148.8
PnP-ISTA	34.29	199	14.5	34.52	200	14.4	34.09	199	14.8	32.78	199	14.3	31.70	199	14.4
	34.30	200	14.6	34.52	200	14.4	34.10	200	14.9	32.79	200	14.4	31.71	200	14.5
P ² nP-F-1	34.32	76	10.4	34.53	76	10.5	34.10	76	10.7	32.82	80	10.9	31.72	79	10.8
	36.00	200	27.4	36.17	200	27.5	35.91	200	28.2	34.85	200	27.1	33.74	200	27.4
P ² nP-F-Cheb	34.33	37	5.1	34.55	37	5.2	34.13	37	5.2	32.84	39	5.3	31.72	38	5.2
	37.37	200	27.4	37.57	200	28.1	37.38	200	27.1	36.65	200	27.1	35.9	200	27.4
P ² nP-D	34.41	28	2.0	34.59	24	1.8	34.11	20	1.5	32.87	19	1.4	31.74	33	2.4
	37.40	200	14.5	38.02	200	14.9	38.01	200	14.8	37.43	200	14.4	36.53	200	14.5

TABLE II

PERFORMANCE OF EACH METHOD ON THE RECONSTRUCTION OF OTHER KNEE TEST IMAGES WITH THE RADIAL ACQUISITION. THE DEFINITION OF DIGITS HERE IS IDENTICAL TO TABLE I. “—” MEANS THE METHOD CANNOT REACH HIGHER PSNR THAN ADMM IN 200 ITERATIONS.

Index	2			3			4			5			6		
	PSNR↑	iter.↓	sec.↓	PSNR↑	iter.↓	sec.↓	PSNR↑	iter.↓	sec.↓	PSNR↑	iter.↓	sec.↓	PSNR↑	iter.↓	sec.↓
PnP-ADMM	35.30	153	106.1	31.17	196	145.4	33.64	176	122	31.36	160	120.4	34.77	150	111.5
PnP-ISTA	—	—	—	31.17	200	14.5	—	—	—	31.36	154	11.3	34.77	145	10.4
	35.16	200	14.5	31.17	200	14.5	33.60	200	14.6	31.21	200	14.6	34.55	200	14.3
P ² nP-F-1	35.30	54	7.4	31.18	72	9.8	33.64	62	8.5	31.38	57	7.9	34.77	52	7.1
	35.62	200	27.3	31.98	200	27.4	34.16	200	27.5	31.89	200	27.6	35.13	200	27.3
P ² nP-F-Cheb	35.30	26	3.5	31.18	35	4.8	33.64	30	4.1	31.42	28	3.8	34.77	25	3.4
	36.01	200	27.3	32.67	200	27.6	34.62	200	27.5	32.45	200	27.7	35.54	200	27.4
P ² nP-D	35.38	19	1.4	31.20	20	1.5	33.76	19	1.4	31.76	17	1.3	34.85	20	1.5
	35.95	200	14.6	32.56	200	14.6	34.27	200	14.7	33.11	200	14.6	36.06	200	14.5

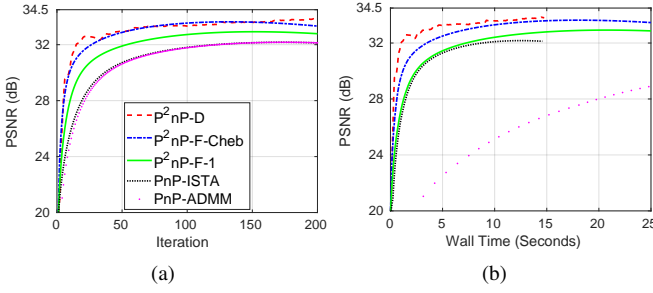


Fig. 5. PSNR values versus iteration and wall (GPU) time on the knee 1 image with radial acquisition.

We used $\rho_k \triangleq (\|\mathbf{x}_{k+1} - \mathbf{x}_k\|_2 / \|\mathbf{x}_2 - \mathbf{x}_1\|_2)^{1/k}$ for $k \geq 1$ to measure the empirical convergence rate, where $\rho_k < 1$ means $\|\mathbf{x}_{k+1} - \mathbf{x}_k\|_2$ tends to zero. Figure 8 shows ρ_k versus iteration for PnP-ISTA and P²nP with fixed and dynamic preconditioners.

D. Comparing Ordinary and Normalization-Equivariant Denoisers

Figure 9 compares the PSNR values of PnP-ISTA on the brain test images with ordinary and normalization-equivariant (“Norm-Equiv”) denoisers. PnP-ISTA with the “Norm-Equiv” denoiser had significantly higher PSNR than the ordinary denoiser and was more robust to running more iterations. This is due to the fact that, compared with ordinary denoisers, the “Norm-Equiv” ones are more robust and adaptive to noise level changes [62]. Ref. [61], illustrated the importance of choosing the proper noise level for the denoiser in the PnP framework. Our experiments demonstrated that the “Norm-Equiv” denoiser can be an appealing choice to automatically address this concern.

V. CONCLUSION

In this paper, we proposed a preconditioned PnP method (P²nP) with provable convergence. We showed that P²nP can significantly accelerate the convergence speed of its no-preconditioner-based counterparts in the reconstruction of CS MRI. Since the forward model in CS MRI is patient-specific, we proposed two different strategies (fixed and dynamic) for computing preconditioners efficiently. The corresponding numerical experiments demonstrated effectiveness and efficiency

of using preconditioners for accelerating MRI reconstruction with spiral and radial trajectories. Moreover, we introduced the use of normalization-equivariant denoisers in the PnP framework. We showed that by providing a self-adaptive way of addressing the noise-level tuning problem in PnP, using normalization-equivariant denoisers not only allows for “solving” (8) but also significantly improves the reconstruction PSNR.

The dynamic preconditioner does not require any explicit knowledge of the forward model, making it a potentially efficient solver for addressing nonlinear inverse problems with PnP, e.g., full waveform inversion [66]. Another promising direction is to unroll P²nP, which may yield a more efficient network than others for image reconstruction. We leave the further investigation of these topics to future work.

APPENDIX A PROOF OF THEOREM 1

The updating scheme in Algorithm 1 can be written as

$$\mathbf{x}_{k+1} = T(\mathbf{x}_k) \text{ with } T(\mathbf{x}) \triangleq \mathbf{D}_\sigma(\mathbf{x} - \alpha \mathbf{P} \nabla f(\mathbf{x})).$$

From the Banach fixed-point theorem, Algorithm 1 is guaranteed to converge to a fixed-point if the mapping $T(\mathbf{x})$ is contractive. So if \mathbf{x}_* is a fixed-point of $T(\mathbf{x})$ such that $\mathbf{x}_* = T(\mathbf{x}_*)$, then conditioned on Assumption 1, we have

$$\begin{aligned} \|\mathbf{x}_{k+1} - \mathbf{x}_*\| &= \|T(\mathbf{x}_k) - T(\mathbf{x}_*)\| \\ &= \|\mathbf{D}_\sigma(\mathbf{x}_k - \alpha \mathbf{P} \nabla f(\mathbf{x}_k)) - \mathbf{D}_\sigma(\mathbf{x}_* - \alpha \mathbf{P} \nabla f(\mathbf{x}_*))\| \\ &\leq (1 + \epsilon) \|\mathbf{x}_k - \mathbf{x}_*\| \\ &\quad - \alpha \mathbf{P} (\nabla f(\mathbf{x}_k) - \nabla f(\mathbf{x}_*)) \| \\ &= (1 + \epsilon) \|\mathbf{x}_k - \mathbf{x}_* - \alpha \mathbf{P} \mathbf{A}^H \mathbf{A} (\mathbf{x}_k - \mathbf{x}_*)\| \\ &\leq (1 + \epsilon) \|\mathbf{I} - \alpha \mathbf{P} \mathbf{A}^H \mathbf{A}\| \cdot \|\mathbf{x}_k - \mathbf{x}_*\|. \end{aligned}$$

Clearly, if $(1 + \epsilon)\rho(\mathbf{I} - \alpha \mathbf{P} \mathbf{A}^H \mathbf{A}) < 1$, the iterates from Algorithm 1 are guaranteed to converge and the convergence rate is at most $(1 + \epsilon)\rho(\mathbf{I} - \alpha \mathbf{P} \mathbf{A}^H \mathbf{A})$.

APPENDIX B PROOF OF LEMMA 1

The proof that τ_k and $\langle \mathbf{s}_k, \mathbf{v}_k \rangle$ are real comes from [7, Observation 1]. Using the fact $\nabla f(\mathbf{x}) = \mathbf{A}^H(\mathbf{A}\mathbf{x} - \mathbf{y})$ and

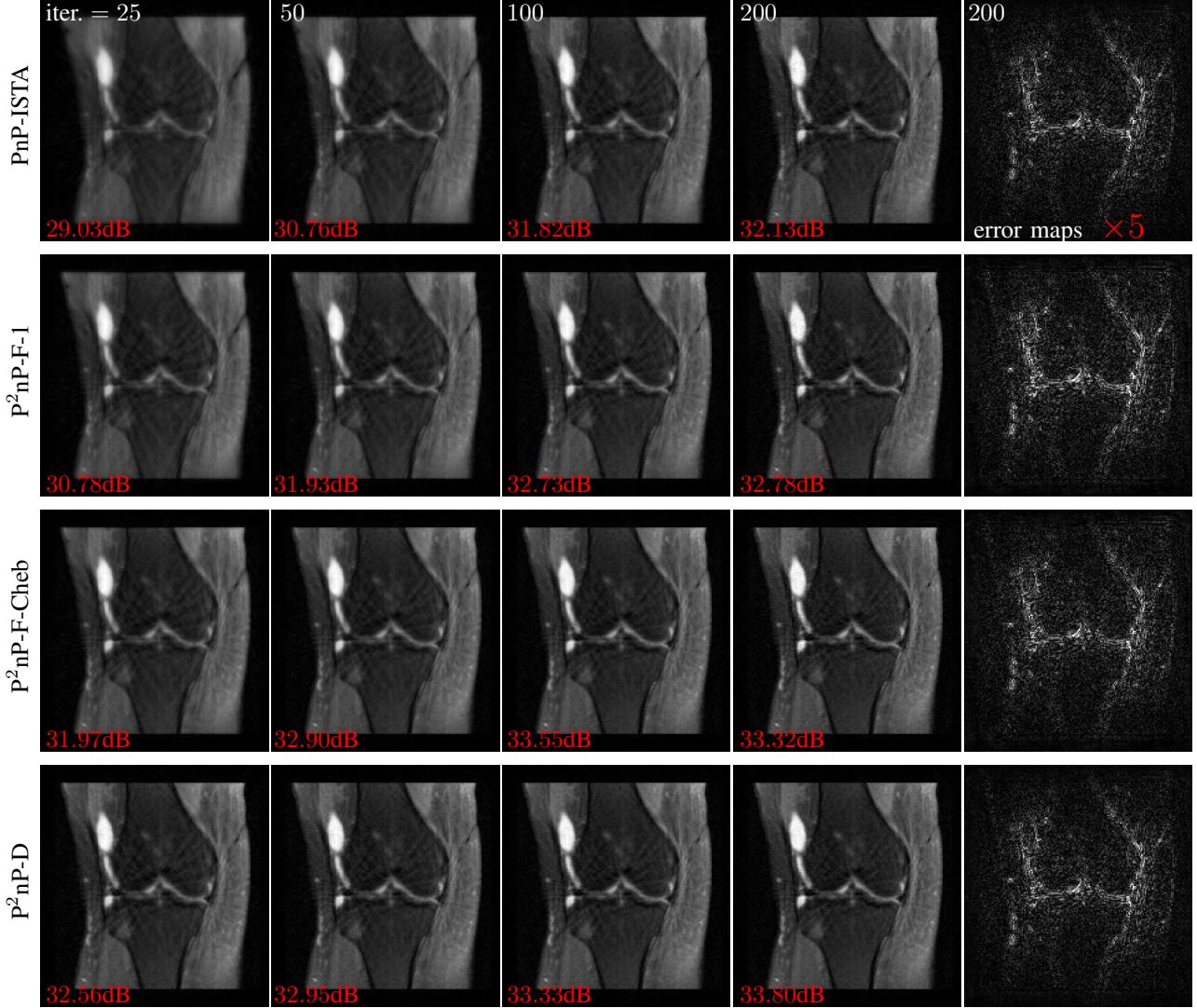


Fig. 6. The reconstructed knee 1 images at 25, 50, 100, 200th iteration with radial acquisition. The PSNR value is labeled in the left bottom corner of each image. The fifth column shown the error maps ($\times 5$) of the reconstructed images at 200th iteration.

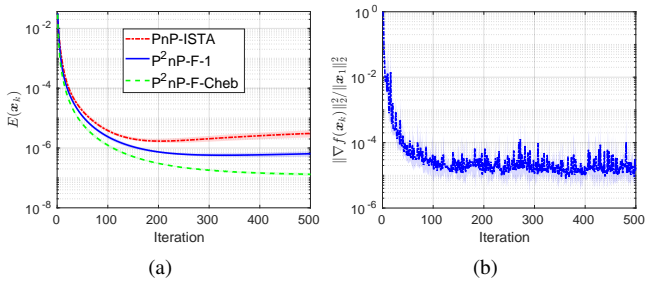


Fig. 7. (a) Numerical test of the fixed-point convergence of PnP-ISTA, P²nP-F-1, and P²nP-F-Cheb. (b) $\|\nabla f(x_k)\|$ values versus iteration for P²nP-D.

following the deduction in [60, Lemma A.3 and Theorem 4.2], we can easily prove that $\langle s_k - \tau_k v_k, v_k \rangle$ is nonnegative and

the bounds of τ_k and P_k so that we omit the details here. The bound of P_k obtained here is much tighter than the one shown in [60, Thm. 4.2] that bound depends on the image size while ours does not. If one considers general nonlinear inverse problems in the complex plane, then Lemma 1 in general is invalid.

APPENDIX C PROOF OF THEOREM 2

The updating scheme of Algorithm 3 at the k th iteration can be represented as

$$\mathbf{x}_{k+1} = T_k(\mathbf{x}_k) \text{ with } T_k(\mathbf{x}) = D_\sigma(\mathbf{x} - \alpha P_k \nabla f(\mathbf{x})).$$

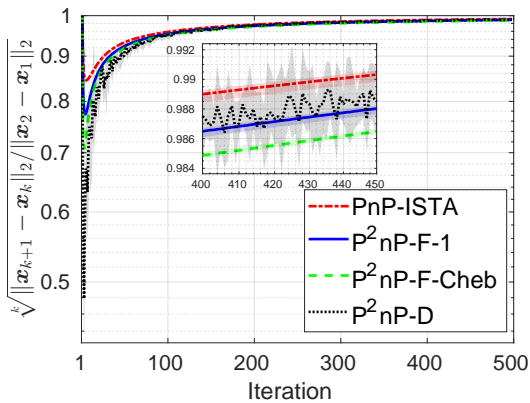


Fig. 8. Numerical test of the convergence rates of PnP-ISTA, P²nP-F-1, P²nP-F-Cheb, and P²nP-D averaged on six brain test images with spiral acquisition. The shaded region of each curve represents the bound of the ρ_k across all brain test images.

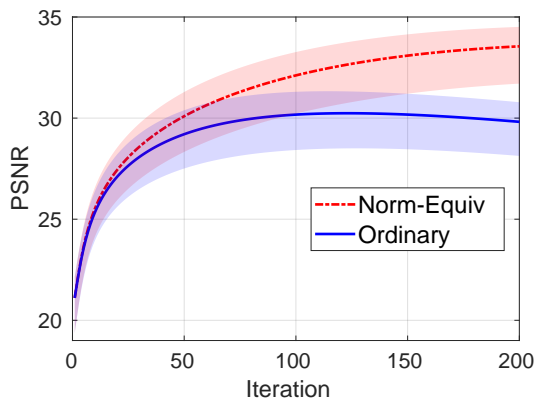


Fig. 9. Averaged PSNR values versus iteration for PnP-ISTA with the normalization-equivariant and ordinary denoisers. The shaded region of each curve represents the bound of the PSNR across all brain test images with spiral acquisition.

Then we have

$$\begin{aligned}
\|\mathbf{x}_{k+1} - \mathbf{x}_*\| &\leq (1 + \epsilon)\|\mathbf{x}_k - \mathbf{x}_*\| \\
&\quad - \alpha(\mathbf{P}_k \nabla f(\mathbf{x}_k) - \mathbf{P}_* \nabla f(\mathbf{x}_*))\| \\
&\leq (1 + \epsilon)\|\mathbf{I} - \alpha \mathbf{P}_* \mathbf{A}^H \mathbf{A}\|\|\mathbf{x}_k - \mathbf{x}_*\| \\
&\quad + (1 + \epsilon)\alpha\|(\mathbf{P}_k - \mathbf{P}_*) \nabla f(\mathbf{x}_k)\| \\
&\leq q^k \|\mathbf{x}_1 - \mathbf{x}_*\| \\
&\quad + (1 + \epsilon)\alpha \sum_{m=1}^k q^{k-m} \|(\mathbf{P}_m \\
&\quad \quad - \mathbf{P}_*) \nabla f(\mathbf{x}_m)\| \\
&\leq q^k \|\mathbf{x}_1 - \mathbf{x}_*\| \\
&\quad + (1 + \epsilon)\alpha R \beta \sum_{m=1}^k q^{k-m} \\
&\leq q^k \|\mathbf{x}_1 - \mathbf{x}_*\| + (1 + \epsilon) \frac{\alpha R \beta}{1 - q}
\end{aligned}$$

where $q \triangleq [(1 + \epsilon)\rho(\mathbf{I} - \alpha \mathbf{P}_* \mathbf{A}^H \mathbf{A})]$ and $\beta \triangleq \max_{m \leq k} \|\mathbf{P}_m - \mathbf{P}_*\| \leq \max_{m \leq k} \|\mathbf{P}_m\| + \|\mathbf{P}_*\| \leq \frac{\delta+1}{\delta\theta_1} + \lambda_*$. The first inequality is the result of Assumption 1. The second inequality derives from the triangle and Cauchy-Schwarz inequalities. The third inequality is obtained by applying first

and second inequalities recursively. The fourth inequality comes from the definitions of R and β .

REFERENCES

- [1] K. P. Pruessmann, M. Weiger, M. B. Scheidegger, and P. Boesiger, "SENSE: sensitivity encoding for fast MRI," *Magnetic Resonance in Medicine*, vol. 42, no. 5, pp. 952–962, 1999.
- [2] M. A. Griswold, P. M. Jakob, R. M. Heidemann, M. Nittka, V. Jellus, J. Wang, B. Kiefer, and A. Haase, "Generalized autocalibrating partially parallel acquisitions (GRAPPA)," *Magnetic Resonance in Medicine*, vol. 47, no. 6, pp. 1202–1210, 2002.
- [3] A. Deshmane, V. Gulani, M. A. Griswold, and N. Seiberlich, "Parallel MR imaging," *Journal of Magnetic Resonance Imaging*, vol. 36, no. 1, pp. 55–72, 2012.
- [4] M. Lustig, D. Donoho, and J. M. Pauly, "Sparse MRI: The application of compressed sensing for rapid MR imaging," *Magnetic Resonance in Medicine*, vol. 58, no. 6, pp. 1182–1195, 2007.
- [5] M. Lustig, D. L. Donoho, J. M. Santos, and J. M. Pauly, "Compressed sensing MRI," *IEEE Signal Processing Magazine*, vol. 25, no. 2, pp. 72–82, 2008.
- [6] L. I. Rudin, S. Osher, and E. Fatemi, "Nonlinear total variation based noise removal algorithms," *Physica D: Nonlinear Phenomena*, vol. 60, no. 1-4, pp. 259–268, 1992.
- [7] T. Hong, L. Hernandez-Garcia, and J. A. Fessler, "A complex quasi-Newton proximal method for image reconstruction in compressed sensing MRI," *IEEE Transactions on Computational Imaging*, vol. 10, pp. 372 – 384, Feb. 2024.
- [8] M. Guerquin-Kern, M. Haberlin, K. P. Pruessmann, and M. Unser, "A fast wavelet-based reconstruction method for magnetic resonance imaging," *IEEE Transactions on Medical Imaging*, vol. 30, no. 9, pp. 1649–1660, 2011.
- [9] M. V. Zibetti, E. S. Helou, R. R. Regatte, and G. T. Herman, "Monotone FISTA with variable acceleration for compressed sensing magnetic resonance imaging," *IEEE Transactions on Computational Imaging*, vol. 5, no. 1, pp. 109–119, 2018.
- [10] M. Aharon, M. Elad, and A. Bruckstein, "K-SVD: An algorithm for designing overcomplete dictionaries for sparse representation," *IEEE Transactions on Signal Processing*, vol. 54, no. 11, pp. 4311–4322, 2006.
- [11] S. Ravishankar and Y. Bresler, "MR image reconstruction from highly undersampled k-space data by dictionary learning," *IEEE Transactions on Medical Imaging*, vol. 30, no. 5, pp. 1028–1041, 2011.
- [12] W. Dong, G. Shi, X. Li, Y. Ma, and F. Huang, "Compressive sensing via nonlocal low-rank regularization," *IEEE Transactions on Image Processing*, vol. 23, no. 8, pp. 3618–3632, 2014.
- [13] J. A. Fessler, "Model-based image reconstruction for MRI," *IEEE Signal Processing Magazine*, vol. 27, no. 4, pp. 81–9, Jul. 2010.
- [14] —, "Optimization methods for magnetic resonance image reconstruction: Key models and optimization al-

- gorithms,” *IEEE Signal Processing Magazine*, vol. 37, no. 1, pp. 33–40, 2020.
- [15] S. Wang, Z. Su, L. Ying, X. Peng, S. Zhu, F. Liang, D. Feng, and D. Liang, “Accelerating magnetic resonance imaging via deep learning,” in *IEEE 13th International Symposium on Biomedical Imaging (ISBI)*. IEEE, 2016, pp. 514–517.
- [16] H. K. Aggarwal, M. P. Mani, and M. Jacob, “MoDL: Model-based deep learning architecture for inverse problems,” *IEEE Transactions on Medical Imaging*, vol. 38, no. 2, pp. 394–405, 2018.
- [17] D. Gilton, G. Ongie, and R. Willett, “Deep equilibrium architectures for inverse problems in imaging,” *IEEE Transactions on Computational Imaging*, vol. 7, pp. 1123–1133, 2021.
- [18] T. Chen, X. Chen, W. Chen, H. Heaton, J. Liu, Z. Wang, and W. Yin, “Learning to optimize: A primer and a benchmark,” *Journal of Machine Learning Research*, vol. 23, no. 189, pp. 1–59, 2022.
- [19] Y. Song, L. Shen, L. Xing, and S. Ermon, “Solving inverse problems in medical imaging with score-based generative models,” in *International Conference on Learning Representations*, 2021.
- [20] H. Chung and J. C. Ye, “Score-based diffusion models for accelerated mri,” *Medical Image Analysis*, vol. 80, p. 102479, 2022.
- [21] S. V. Venkatakrishnan, C. A. Bouman, and B. Wohlberg, “Plug-and-play priors for model based reconstruction,” in *IEEE Global Conference on Signal and Information Processing*. IEEE, 2013, pp. 945–948.
- [22] K. Dabov, A. Foi, V. Katkovnik, and K. Egiazarian, “Image denoising by sparse 3-D transform-domain collaborative filtering,” *IEEE Transactions on Image Processing*, vol. 16, no. 8, pp. 2080–2095, 2007.
- [23] K. Zhang, W. Zuo, Y. Chen, D. Meng, and L. Zhang, “Beyond a Gaussian denoiser: Residual learning of deep cnn for image denoising,” *IEEE Transactions on Image Processing*, vol. 26, no. 7, pp. 3142–3155, 2017.
- [24] S. Sreehari, S. V. Venkatakrishnan, B. Wohlberg, G. T. Buzzard, L. F. Drummy, J. P. Simmons, and C. A. Bouman, “Plug-and-play priors for bright field electron tomography and sparse interpolation,” *IEEE Transactions on Computational Imaging*, vol. 2, no. 4, pp. 408–423, 2016.
- [25] S. Ono, “Primal-dual plug-and-play image restoration,” *IEEE Signal Processing Letters*, vol. 24, no. 8, pp. 1108–1112, 2017.
- [26] T. Meinhardt, M. Moeller, C. Hazirbas, and D. Cremers, “Learning proximal operators: Using denoising networks for regularizing inverse imaging problems,” in *Proceedings of the IEEE International Conference on Computer Vision*, Venice, Italy, Oct. 2017, pp. 1799–1808.
- [27] G. T. Buzzard, S. H. Chan, S. Sreehari, and C. A. Bouman, “Plug-and-Play unplugged: Optimization free reconstruction using consensus equilibrium,” *SIAM Journal on Imaging Sciences*, vol. 11, no. 3, pp. 2001–2020, 2018.
- [28] W. Dong, P. Wang, W. Yin, G. Shi, F. Wu, and X. Lu, “Denoising prior driven deep neural network for image restoration,” *IEEE Transactions on Pattern Analysis and Machine Intelligence*, vol. 41, no. 10, p. 2305–2318, Oct. 2019.
- [29] K. Zhang, Y. Li, W. Zuo, L. Zhang, L. Van Gool, and R. Timofte, “Plug-and-play image restoration with deep denoiser prior,” *IEEE Transactions on Pattern Analysis and Machine Intelligence*, vol. 44, no. 10, pp. 6360–6376, 2021.
- [30] R. Ahmad, C. A. Bouman, G. T. Buzzard, S. Chan, S. Liu, E. T. Reehorst, and P. Schniter, “Plug-and-play methods for magnetic resonance imaging: Using denoisers for image recovery,” *IEEE Signal Processing Magazine*, vol. 37, no. 1, pp. 105–116, 2020.
- [31] N. Parikh, S. Boyd *et al.*, “Proximal algorithms,” *Foundations and Trends® in Optimization*, vol. 1, no. 3, pp. 127–239, 2014.
- [32] A. Beck and M. Teboulle, “A fast iterative shrinkage-thresholding algorithm for linear inverse problems,” *SIAM Journal on Imaging Sciences*, vol. 2, no. 1, pp. 183–202, 2009.
- [33] S. H. Chan, X. Wang, and O. A. Elgendy, “Plug-and-play admm for image restoration: Fixed-point convergence and applications,” *IEEE Transactions on Computational Imaging*, vol. 3, no. 1, pp. 84–98, 2017.
- [34] S. Boyd, N. Parikh, E. Chu, B. Peleato, J. Eckstein *et al.*, “Distributed optimization and statistical learning via the alternating direction method of multipliers,” *Foundations and Trends® in Machine Learning*, vol. 3, no. 1, pp. 1–122, 2011.
- [35] K. Zhang, W. Zuo, S. Gu, and L. Zhang, “Learning deep CNN denoiser prior for image restoration,” in *IEEE Conference on Computer Vision and Pattern Recognition*, 2017, pp. 3929–3938.
- [36] Y. Romano, M. Elad, and P. Milanfar, “The little engine that could: Regularization by denoising (RED),” *SIAM Journal on Imaging Sciences*, vol. 10, no. 4, pp. 1804–1844, 2017.
- [37] T. Hong, Y. Romano, and M. Elad, “Acceleration of RED via vector extrapolation,” *Journal of Visual Communication and Image Representation*, p. 102575, 2019.
- [38] E. T. Reehorst and P. Schniter, “Regularization by denoising: Clarifications and new interpretations,” *IEEE Transactions on Computational Imaging*, vol. 5, no. 1, pp. 52–67, 2019.
- [39] H. Y. Tan, S. Mukherjee, J. Tang, and C.-B. Schönlieb, “Provably convergent plug-and-play quasi-Newton methods,” *SIAM Journal on Imaging Sciences*, vol. 17, no. 2, pp. 785–819, 2024.
- [40] M. L. Pendu and C. Guillemot, “Preconditioned plug-and-play ADMM with locally adjustable denoiser for image restoration,” *SIAM Journal on Imaging Sciences*, vol. 16, no. 1, pp. 393–422, 2023.
- [41] A. M. Teodoro, J. M. Bioucas-Dias, and M. A. T. Figueiredo, “A convergent image fusion algorithm using scene-adapted gaussian-mixture-based denoising,” *IEEE Transactions on Image Processing*, vol. 28, no. 1, pp. 451–463, Jan. 2019.

- [42] R. G. Gavaskar, C. D. Athalye, and K. N. Chaudhury, "On plug-and-play regularization using linear denoisers," *IEEE Transactions on Image Processing*, vol. 30, pp. 4802–4813, 2021.
- [43] Y. Sun, B. Wohlberg, and U. S. Kamilov, "An online plug-and-play algorithm for regularized image reconstruction," *IEEE Transactions on Computational Imaging*, vol. 5, no. 3, pp. 395–408, Sep. 2019.
- [44] E. Ryu, J. Liu, S. Wang, X. Chen, Z. Wang, and W. Yin, "Plug-and-play methods provably converge with properly trained denoisers," in *International Conference on Machine Learning*. PMLR, 2019, pp. 5546–5557.
- [45] Y. Sun, Z. Wu, X. Xu, B. Wohlberg, and U. S. Kamilov, "Scalable plug-and-play ADMM with convergence guarantees," *IEEE Transactions on Computational Imaging*, vol. 7, pp. 849–863, 2021.
- [46] M. Terris, A. Repetti, J.-C. Pesquet, and Y. Wiaux, "Building firmly nonexpansive convolutional neural networks," in *ICASSP 2020-2020 IEEE International Conference on Acoustics, Speech and Signal Processing (ICASSP)*. IEEE, 2020, pp. 8658–8662.
- [47] X. Xu, Y. Sun, J. Liu, B. Wohlberg, and U. S. Kamilov, "Provable convergence of plug-and-play priors with MMSE denoisers," *IEEE Signal Processing Letters*, vol. 27, pp. 1280–1284, 2020.
- [48] J. Liu, S. Asif, B. Wohlberg, and U. Kamilov, "Recovery analysis for plug-and-play priors using the restricted eigenvalue condition," *Advances in Neural Information Processing Systems*, vol. 34, pp. 5921–5933, 2021.
- [49] R. Cohen, M. Elad, and P. Milanfar, "Regularization by denoising via fixed-point projection (RED-PRO)," *SIAM Journal on Imaging Sciences*, vol. 14, no. 3, pp. 1374–1406, 2021.
- [50] U. S. Kamilov, C. A. Bouman, G. T. Buzzard, and B. Wohlberg, "Plug-and-play methods for integrating physical and learned models in computational imaging: Theory, algorithms, and applications," *IEEE Signal Processing Magazine*, vol. 40, no. 1, pp. 85–97, 2023.
- [51] Z. Aminifard and S. Babaie-Kafaki, "An approximate Newton-type proximal method using symmetric rank-one updating formula for minimizing the nonsmooth composite functions," *Optimization Methods and Software*, vol. 38, no. 3, pp. 529–542, 2023.
- [52] M. J. Grote and T. Huckle, "Parallel preconditioning with sparse approximate inverses," *SIAM Journal on Scientific Computing*, vol. 18, no. 3, pp. 838–853, 1997.
- [53] N. I. Gould and J. A. Scott, "Sparse approximate-inverse preconditioners using norm-minimization techniques," *SIAM Journal on Scientific Computing*, vol. 19, no. 2, pp. 605–625, 1998.
- [54] O. G. Johnson, C. A. Micchelli, and G. Paul, "Polynomial preconditioners for conjugate gradient calculations," *SIAM Journal on Numerical Analysis*, vol. 20, no. 2, pp. 362–376, 1983.
- [55] M. Zulfiquar Ali Bhotto, M. O. Ahmad, and M. Swamy, "An improved fast iterative shrinkage thresholding algorithm for image deblurring," *SIAM Journal on Imaging Sciences*, vol. 8, no. 3, pp. 1640–1657, 2015.
- [56] S. S. Iyer, F. Ong, X. Cao, C. Liao, L. Daniel, J. I. Tamir, and K. Setsompop, "Polynomial preconditioners for regularized linear inverse problems," *SIAM Journal on Imaging Sciences*, vol. 17, no. 1, pp. 116–146, 2024.
- [57] J. Nocedal and S. J. Wright, *Numerical Optimization*. Springer, 2006.
- [58] M. Osborne and L. Sun, "A new approach to symmetric rank-one updating," *IMA Journal of Numerical Analysis*, vol. 19, no. 4, pp. 497–507, 1999.
- [59] F. Curtis, "A self-correcting variable-metric algorithm for stochastic optimization," in *International Conference on Machine Learning*. PMLR, 2016, pp. 632–641.
- [60] X. Wang, X. Wang, and Y.-X. Yuan, "Stochastic proximal quasi-Newton methods for non-convex composite optimization," *Optimization Methods and Software*, vol. 34, no. 5, pp. 922–948, 2019.
- [61] X. Xu, J. Liu, Y. Sun, B. Wohlberg, and U. S. Kamilov, "Boosting the performance of plug-and-play priors via denoiser scaling," in *2020 54th Asilomar Conference on Signals, Systems, and Computers*. IEEE, 2020, pp. 1305–1312.
- [62] S. Herbreteau, E. Moebel, and C. Kervrann, "Normalization-equivariant neural networks with application to image denoising," *Advances in Neural Information Processing Systems*, vol. 36, 2024.
- [63] J. Zbontar, F. Knoll, A. Sriram, T. Murrell, Z. Huang, M. J. Muckley, A. Defazio, R. Stern, P. Johnson, M. Bruno *et al.*, "fastMRI: An open dataset and benchmarks for accelerated MRI," *arXiv preprint arXiv:1811.08839*, 2018.
- [64] M. Uecker, P. Lai, M. J. Murphy, P. Virtue, M. Elad, J. M. Pauly, S. S. Vasanawala, and M. Lustig, "ESPIRiT—an eigenvalue approach to autocalibrating parallel MRI: where SENSE meets GRAPPA," *Magnetic Resonance in Medicine*, vol. 71, no. 3, pp. 990–1001, 2014.
- [65] A. Paszke, S. Gross, F. Massa, A. Lerer, J. Bradbury, G. Chanan, T. Killeen, Z. Lin, N. Gimelshein, L. Antiga *et al.*, "Pytorch: An imperative style, high-performance deep learning library," *Advances in Neural Information Processing Systems*, vol. 32, 2019.
- [66] L. Métivier, R. Brossier, J. Virieux, and S. Operto, "Full waveform inversion and the truncated Newton method," *SIAM Journal on Scientific Computing*, vol. 35, no. 2, pp. B401–B437, 2013.

Supplementary Material: Provable Preconditioned Plug-and-Play Approach for Compressed Sensing MRI Reconstruction

Tao Hong, *Member, IEEE*, Xiaojian Xu, *Member, IEEE*, Jason Hu, *Student Member, IEEE*, and Jeffrey A. Fessler, *Fellow, IEEE*

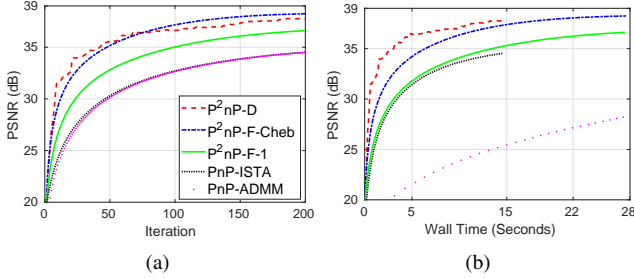


Fig. S.1. PSNR values versus iteration and wall (GPU) time for the knee 1 test image with spiral acquisition.

S.I. SPIRAL ACQUISITION RECONSTRUCTION

Figure S.1 presents the PSNR values versus iteration and wall time for the knee 1 image with spiral acquisition. Clearly, we saw P^2nP -F-1/Cheb and P^2nP -D converged faster than PnP-ISTA and PnP-ADMM in terms of iteration number and wall time. Moreover, we observed P^2nP -D was faster than P^2nP -F-Cheb in terms of wall time, but P^2nP -F-Cheb achieved higher PSNR eventually. In this setting, P^2nP -F-1 was only slightly faster than PnP-ISTA and PnP-ADMM in terms of wall time. Figure S.2 shows the reconstructed images of each method. Obviously, P^2nP required less iterations to achieve higher PSNR than PnP-ISTA and PnP-ADMM, illustrating the effectiveness of using preconditioners. Table S.I describes the results of other knee test images. Evidently, similar trend was observed for the brain test images.

S.II. RADIAL ACQUISITION RECONSTRUCTION

Figure S.3 describes the PSNR values versus iteration and wall time of the brain 1 test image with radial acquisition. From Figure S.3, we observed P^2nP converged faster than PnP-ISTA and PnP-ADMM. Moreover, P^2nP -D converged similar to P^2nP -F-Cheb in terms of iteration but P^2nP -D was faster than P^2nP -F-Cheb in terms of wall time. Table S.II shows the results of other test images, illustrating the effectiveness of adding preconditioners.

T. Hong is with the Department of Radiology, University of Michigan, Ann Arbor, MI 48109, USA (Email: tahong@umich.edu). TH was partly supported by National Institutes of Health grant R01NS112233.

J. Hu, X. Xu and J. Fessler are with the Department of Electrical and Computer Engineering, University of Michigan, Ann Arbor, MI 48109, USA (Email: {jashu, xjxu, fessler}@umich.edu).

S.III. RADIAL ACQUISITION RECONSTRUCTION WITH 55 SPOKES

Figure S.5 describes the reconstruction of knee 1 test image with the 55 spokes radial acquisition. Clearly, the undesired artifacts in the 21 spokes radial acquisition disappeared and P^2nP -D yielded the highest PSNR at 200th iteration.

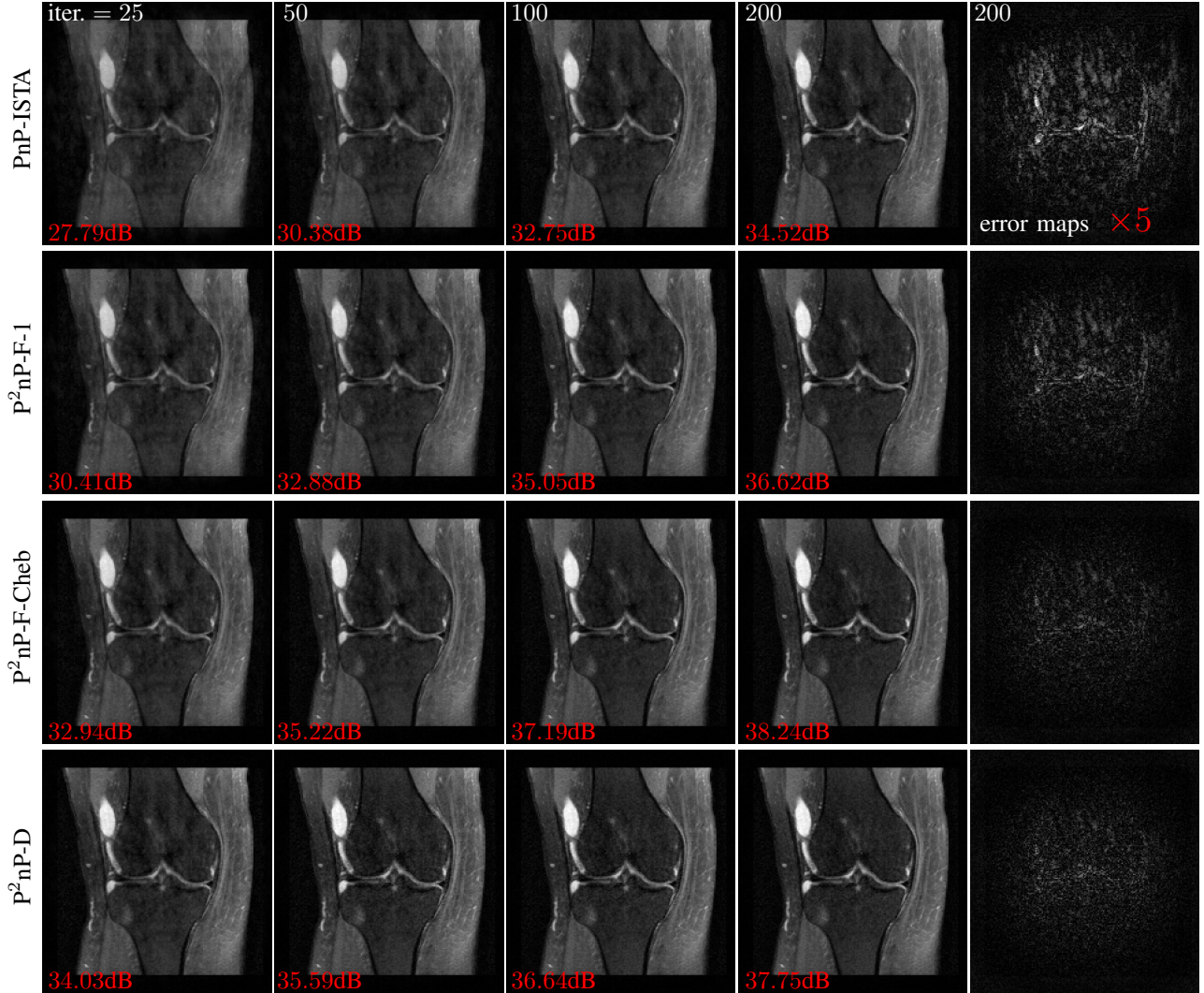


Fig. S.2. The reconstructed knee 1 images at 25, 50, 100, 200th iteration with spiral acquisition. The PSNR value is labeled in the left bottom corner of each image. The fifth column shown the error maps ($\times 5$) of the reconstructed images at 200th iteration. We omitted the PnP-ADMM results since it is similar to PnP-ISTA.

TABLE S.1

PSNR PERFORMANCE OF EACH METHOD FOR RECONSTRUCTING 5 OTHER BRAIN TEST IMAGES WITH SPIRAL ACQUISITION. FOR PnP-ADMM, WE SHOWED THE MAXIMAL PSNR AND THE ASSOCIATED NUMBER OF ITERATIONS, AND WALL TIME THAT IS USED AS THE BENCHMARK. FOR OTHER METHODS ON EACH TEST IMAGE, THE SECOND COLUMN OF THE FIRST ROW REPRESENTS THE FIRST ITERATION THAT EXCEEDED PnP-ADMM PSNR. THE RELATED FIRST AND THIRD COLUMNS ARE THE ASSOCIATED PSNR AND WALL TIME, RESPECTIVELY. THE **BOLD** DIGITS DENOTE THE NUMBER OF ITERATIONS AND WALL TIME OF THE FASTEST ALGORITHM THAT FIRST EXCEEDED PnP-ADMM. THE SECOND ROW SHOWS THE PSNR AND WALL TIME AT THE 200TH ITERATION. THE **BLUE** DIGITS DENOTE THE HIGHEST PSNR AT THE 200TH ITERATION.

Index	2			3			4			5			6		
	PSNR \uparrow	iter. \downarrow	sec. \downarrow	PSNR \uparrow	iter. \downarrow	sec. \downarrow	PSNR \uparrow	iter. \downarrow	sec. \downarrow	PSNR \uparrow	iter. \downarrow	sec. \downarrow	PSNR \uparrow	iter. \downarrow	sec. \downarrow
PnP-ADMM	37.85	200	147.8	34.33	200	148	34.96	200	147.4	33.53	200	148.9	34.24	200	147.8
PnP-ISTA	37.85	200	14.6	34.33	199	14.6	34.96	199	14.5	33.54	199	14.4	34.25	199	14.5
	37.85	200	14.6	34.34	200	14.7	34.97	200	14.6	33.55	200	14.5	34.26	200	14.6
P ² nP-F-1	37.85	75	10.3	34.36	85	11.7	34.96	84	11.5	33.57	87	11.8	34.27	90	12.3
	39.03	200	27.4	36.43	200	27.5	36.73	200	27.5	35.92	200	27.2	36.44	200	27.4
P ² nP-F-Cheb	37.91	37	5	34.36	41	5.7	34.99	41	5.6	33.56	42	5.7	34.28	44	6.1
	39.66	200	27.5	38.03	200	27.5	38.15	200	27.5	37.77	200	27.4	38.14	200	27.5
P ² nP-D	38.34	36	2.6	34.33	21	1.5	35.06	26	1.9	33.58	35	2.6	34.29	23	1.7
	39.80	200	14.6	38.23	200	14.5	37.90	200	14.8	38.04	200	14.6	38.21	200	14.6

TABLE S.II
 PERFORMANCE OF EACH METHOD ON THE RECONSTRUCTION OF OTHER BRAIN TEST IMAGES WITH RADIAL ACQUISITION. THE DEFINITION OF DIGITS IS IDENTICAL TO TABLE S.I. “—” MEANS THE METHOD CANNOT REACH HIGHER PSNR IN 200 ITERATIONS.

Index Methods	2			3			4			5			6		
	PSNR↑	iter.↓	sec.↓	PSNR↑	iter.↓	sec.↓	PSNR↑	iter.↓	sec.↓	PSNR↑	iter.↓	sec.↓	PSNR↑	iter.↓	sec.↓
PnP-ADMM	30.76	181	134.5	31.31	181	132.7	30.79	182	133.3	29.63	175	129.1	29.23	163	121.8
PnP-ISTA	—	—	—	—	—	—	—	—	—	—	—	—	—	—	—
	30.73	200	14.5	31.29	200	14.3	30.77	200	14.4	29.59	200	14.4	29.14	200	14.4
P ² nP-F-1	30.77	66	9.0	31.31	64	8.7	30.81	65	8.8	29.64	61	8.4	29.24	58	8.0
	31.38	200	27.4	31.95	200	27.3	31.46	200	27.2	30.25	200	27.3	29.67	200	27.5
P ² nP-F-Cheb	30.80	33	4.6	31.35	32	4.4	30.83	32	4.3	29.66	30	4.1	29.23	28	3.8
	31.93	200	27.7	32.50	200	27.3	32.03	200	27.1	30.82	200	27.2	30.13	200	27.3
P ² nP-D	30.77	18	1.3	31.41	24	1.8	30.83	20	1.4	29.66	25	1.8	29.23	27	2.0
	32.07	200	14.7	32.68	200	14.3	32.04	200	14.4	30.51	200	14.5	28.70	200	14.5

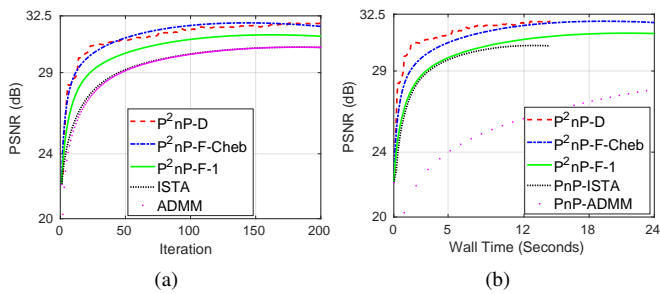


Fig. S.3. PSNR values versus iteration and wall (GPU) time for the brain 1 test image with radial acquisition.

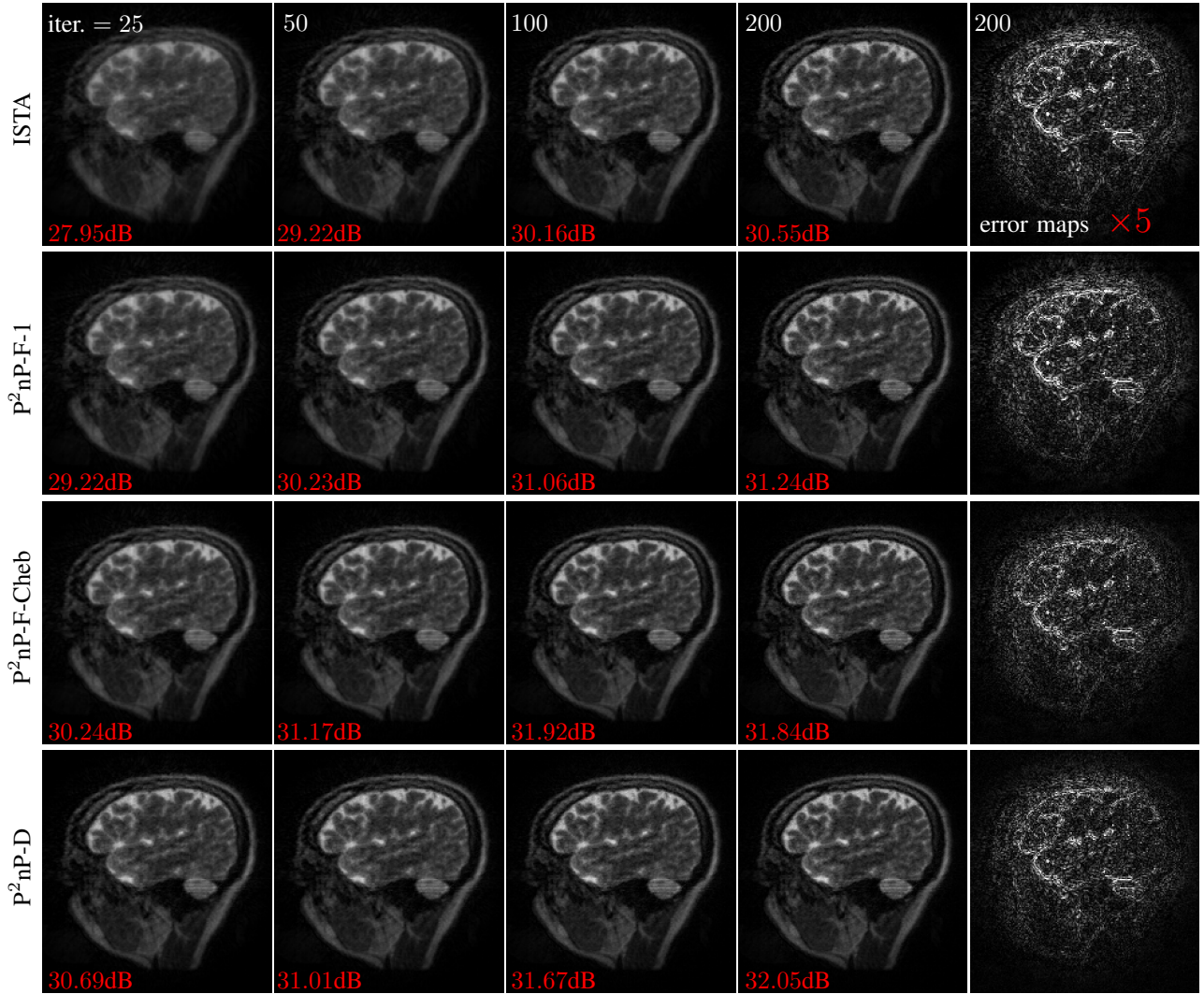


Fig. S.4. The reconstructed brain 1 images at 25, 50, 100, 200th iteration with different algorithms for radial acquisition. The PSNR value is labeled in the left bottom corner of each image. The fifth column shown the error maps ($\times 5$) of the reconstructed images at 200th iteration.

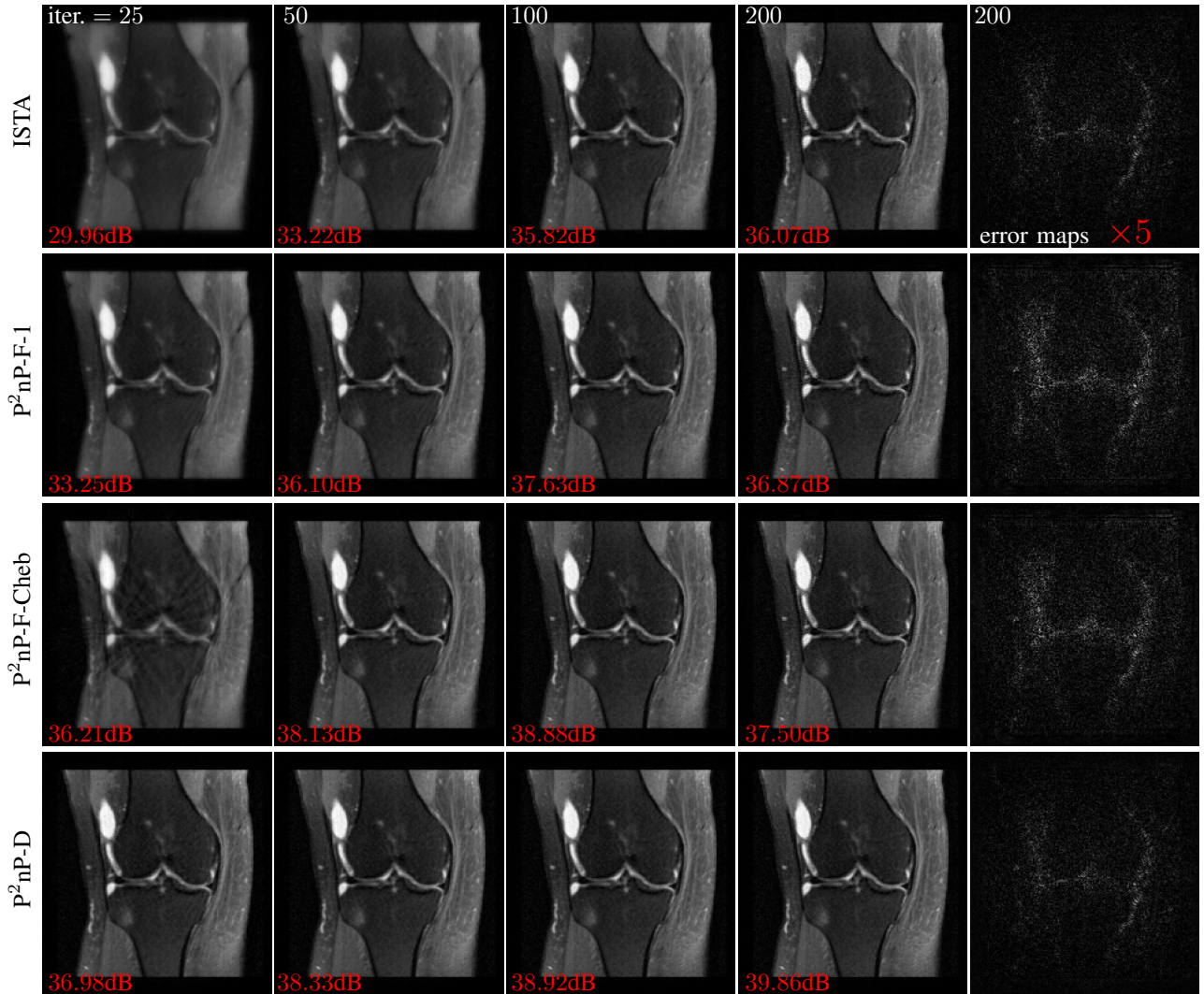


Fig. S.5. The reconstructed knee 1 images at 25, 50, 100, 200th iteration with radial acquisition of 55 spokes. The fifth column shown the error maps ($\times 5$) of the reconstructed images at 200th iteration.